Geophys. J. Int. (2009) **178,** 1565–1573 doi: 10.1111/j.1365-246X.2009.04248.x

Calculation of the wave propagation angle in complex media: application to turning wave simulations

Xiaofeng Jia and Ru-Shan Wu

Modeling and Imaging Laboratory, Institute of Geophysics and Planetary Physics, University of California, Santa Cruz, CA 95064*, USA.*
E-mail: xiaofengdq@gmail.com

Accepted 2009 May 10. Received 2009 May 10; in original form 2008 August 29

SUMMARY

The wave propagation angle is one of the key factors in seismic processing methods. For the dual-domain propagators, it is sometimes necessary to acquire the wave propagation angle in the space-frequency domain instead of the wavenumber domain or the angle domain. We propose a method dealing with this problem, in which the wavefield gradient is used for the calculation of the wave propagation angle. The wavefield gradient can be directly obtained by either the finite difference approximation or the marching expression of the propagator. This method is not applicable in the case of extremely low frequency due to the comparability between the wavelength and the grid interval. Combined with the superwide-angle one-way propagator, this approach is instrumental in simulating the turning wave, which is hard to be handled by the traditional one-way propagator. Numerical examples show the good performance of the superwide-angle one-way propagator with our approach involved. The turning wave is modelled accurately; as a result, a high-quality image of the overhanging salt flank can be obtained.

Key words: Numerical approximations and analysis; Computational seismology; Wave propagation.

1 INTRODUCTION

In the research of seismic exploration, wave motion is essential to understand the theories of modelling, imaging and even signal analysis. Seismic waves propagate in the media, excited from the source or the supposed source such as the receiver array with recorded data. In complex media with strong velocity contrast, the wavefield propagation is quite complicated. In any case, the wavefield at a given space point can be described by the amplitude, the traveltime and the propagating direction. The amplitude and the traveltime describe the ‘state’ of the wavefield while the propagating direction tells its ‘trend’ additionally. The propagating direction, represented by the propagation angle, provides much useful information for seismic processing. It is significant in the problems concerned with anisotropy (Crampin *et al.* 1982; Vines *et al.* 1995; Jones *et al*. 1996). The propagation angle plays an important role in seismic signal filtering and processing (Newman & Mahoney 1973; Roberts & Goulty 1990; Fomel 2002). The amplitude variation with offset (AVO) inversion, where the propagation angle acts as an independent variable, is a powerful tool to indicate hydrocarbon reservoir (Ostrander 1984; Castagna *et al*. 1993; Wapenaar *et al*. 1999). Furthermore, the propagation angle is also one of the basic parameters used in illumination analysis (Wu & Chen 2006; Xie *et al*. 2006). The principle of the propagation angle domain brings a lot of progress in migration and velocity analysis (Rickett & Sava 2002; Biondi & Symes 2004; Zhang *et al*. 2007). Currently the seismic angle migration with dip focusing has been developed which is target-oriented and takes multipathing into account (Ursin *et al*. 2005). In this study, the wavefield propagation angle will be employed by the one-way wave propagator to simulate some special waves, which can hardly be modelled with the original one-way wave propagator.

Ray tracing provides a powerful tool for the calculation of the propagation angle in the high-frequency limit (Aki & Richards 1980; Cerveny 2001; Bruneton *et al*. 2002; Gray 2006; Ruud 2006). The slowness vector indicates the propagation direction of the wave front. Ray-based methods are fast and easy to be conducted. Moreover, beam-based methods give a solution to address the multipathing limitations of the traditional ray theory. However, the propagation angle results of ray methods are difficult to be adopted by the one-way wave propagators most of which are implemented in the frequency domain. It would be advantageous to develop a simple technique in which the propagation angle is obtained from the one-way wave propagator itself.

As the first-order derivative of the displacement in space, the wavefield gradient has been discussed in quite limited literatures. Due to the close relation to material strains, the wavefield gradient is attached importance mainly in some other areas instead of seismic exploration. Jia & Hu (2006) applied the element-free method, which had been proved accurate especially for the displacement gradient in the study of crack growth, to calculate the seismic wavefield. The gradient of the surface displacement can be used for fault plane detections in the earthquake research (Fujiwara *et al*. 2000; Legrand 2003). On the other hand, there are some works dealing with the Poynting vector (Nelson 1996), which has something in common with the wavefield gradient. The Poynting vector indicates the energy flow at a given point. Analyses of the Poynting vector can be found in some anisotropy problems (Mandal & Toksöz 1990; Carcione 1997; Cerveny & Psencik 2006). Yoon & Marfurt (2006) developed a notable application of the Poynting vector in seismic exploration. They calculated the wave propagation direction using the Poynting vector and modified the imaging condition to eliminate some strong directional artefacts from the reverse-time migration result. In this paper, we use the wavefield gradient, instead of the Poynting vector, to determine the wave propagation angle. The applications of this approach will be demonstrated in simulating turning waves and imaging steep reflectors.

2 CALCULATION OF THE WAVEFIELD PROPAGATION ANGLE

The Poynting vector is a measure of energy flow providing a tool to get the wave propagation direction. In the time domain it has the form of

$$\mathbf{P} = -\nabla u \frac{\partial u}{\partial t} u, \tag{1}$$

where u is the pressure in the wavefield, t is the time and ∇ is the gradient operator. For wave propagators developed in the frequency domain, the Poynting vector is hard to be obtained due to the factor of $\partial u/\partial t$. Fortunately, we only need the direction of the Poynting vector to indicate the wave propagation direction. In the case of acoustic waves, the Poynting vector has the same direction as the wavefield gradient according to eq. (1). Therefore, at a given field point, we can use the wavefield gradient to determine the energy flow direction as well as the wave propagation direction.

To obtain the wavefield gradient in the space domain, an easy method is implemented by the finite difference scheme, which gives in the 2-D case

$$\left.\frac{\partial u}{\partial x}\right|_{m,n} = \frac{u_{m,n} - u_{m-1,n}}{\Delta x}, \tag{2}$$

$$\left.\frac{\partial u}{\partial z}\right|_{m,n} = \frac{u_{m,n} - u_{m,n-1}}{\Delta z}, \tag{3}$$

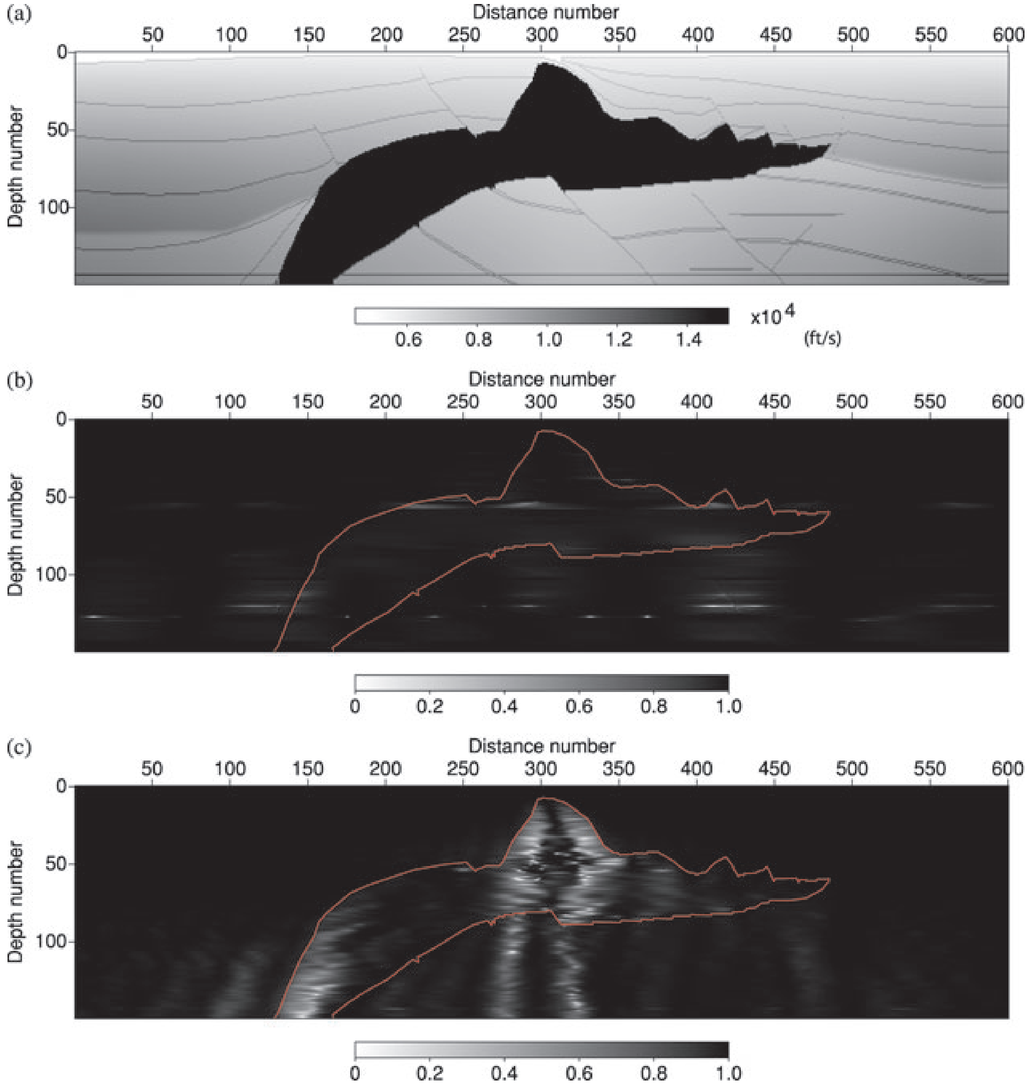

Figure 1. Distribution of $\cos\theta$ for the SEG/EAEG salt model with a vertically propagated plane wave source. (a) The A–A′ profile of the SEG/EAEG salt model. The velocity unit is ft s^{-1}. (b–f) Distribution of $\cos\theta$ for the frequencies of 1, 5, 15, 30 and 100 Hz, respectively. The contour of the salt is illustrated for reference.

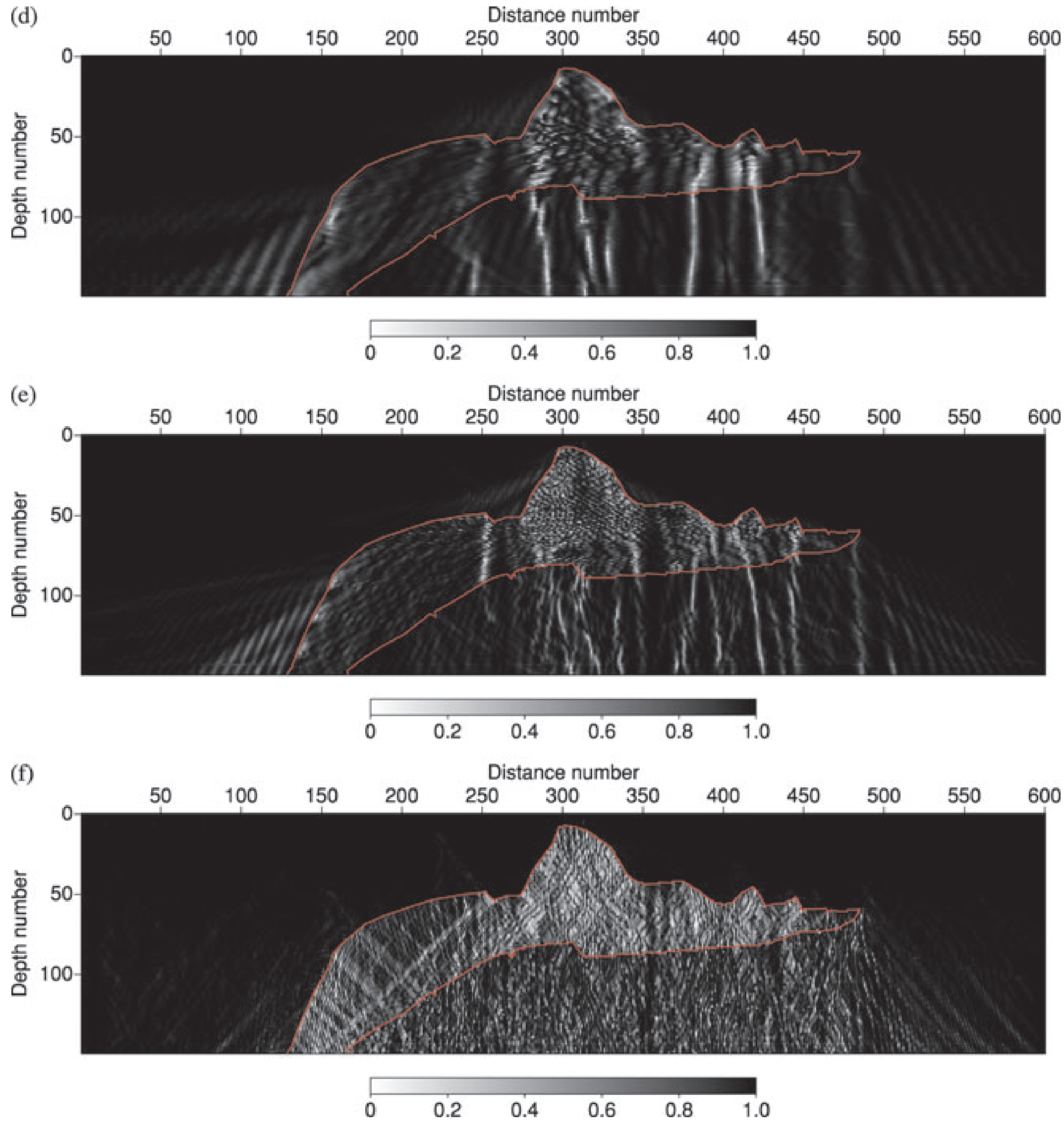

Figure 1. (*Contiued.*)

where x and z are the horizontal and vertical coordinates in space, respectively; Δx and Δz are the corresponding grid intervals and the subscripts m and n stand for the location numbers of the given space point. This finite difference scheme has relatively low computational cost and is applicable to almost any propagators. However, the accuracy of the wavefield gradient obtained with eqs (2) and (3) depends on the grid spacing. Another more stable method to calculate the gradient is deriving its expression directly from the marching equation of the wavefield. In this study, as an example, we use the Padé generalized screen propagator (GSP, Xie & Wu 1998) for the calculation of the wavefield propagation. It is a wide-angle dual-domain one-way propagator and the wavefield can be expressed as

$$u(x,z_1)=\left(\mathrm{F}^{-1}-\mathrm{i}\Delta z k_0 A\mathrm{F}^{-1}\frac{k_x^2}{k_0^2}\right)\mathrm{e}^{\mathrm{i}\Delta z k_z}\mathrm{F}\mathrm{e}^{-\mathrm{i}\Delta z k_0\frac{\delta c}{c}}u(x,z_0), \qquad (4)$$

in which z_0 and z_1 are the vertical coordinates of two adjacent screens, $\delta c/c$ is the relative velocity perturbation, k_0 is the reference or background wavenumber, k_x is the transverse wavenumber, $k_z=\sqrt{k_0^2-k_x^2}$ is the vertical wavenumber, A is a constant and F denotes Fourier transform from the space domain to the wavenumber domain. There are three factors multiplied with $u(x,z_0)$ on the right-hand side of eq. (4). The two exponents describe the background wavefield and the perturbation wavefield, respectively; the factor in the bracket improves the accuracy of the wide-angle wavefield. From eq. (4), we have

$$\frac{\partial u(x,z_1)}{\partial x}=\mathrm{i}\left(\mathrm{F}^{-1}-\mathrm{i}\Delta z k_0 A\mathrm{F}^{-1}\frac{k_x^2}{k_0^2}\right)k_x\mathrm{e}^{\mathrm{i}\Delta z k_z}\mathrm{F}\mathrm{e}^{-\mathrm{i}\Delta z k_0\frac{\delta c}{c}}u(x,z_0). \qquad (5)$$

Based on the unintegrated form of eq. (4), the other component of the wavefield gradient is given by

$$\frac{\partial u(x,z_1)}{\partial z}=\mathrm{i}k_z u(x,z_1)-\mathrm{i}k_0\frac{\delta c}{c}u(x,z_1)+\mathrm{i}\frac{A}{k_0}\frac{\partial^2 u(x,z_1)}{\partial x^2}. \qquad (6)$$

Eqs (5) and (6) provide an accurate but relatively time-consuming approach of calculating the wavefield gradient, compared with eqs (2) and (3). Once the gradient vector is obtained, we have the propagation angle with respect to the vertical direction as

$$\theta(x,z)=\tan^{-1}\left(\left|\frac{\partial u}{\partial x}\right|\Big/\left|\frac{\partial u}{\partial z}\right|\right). \qquad (7)$$

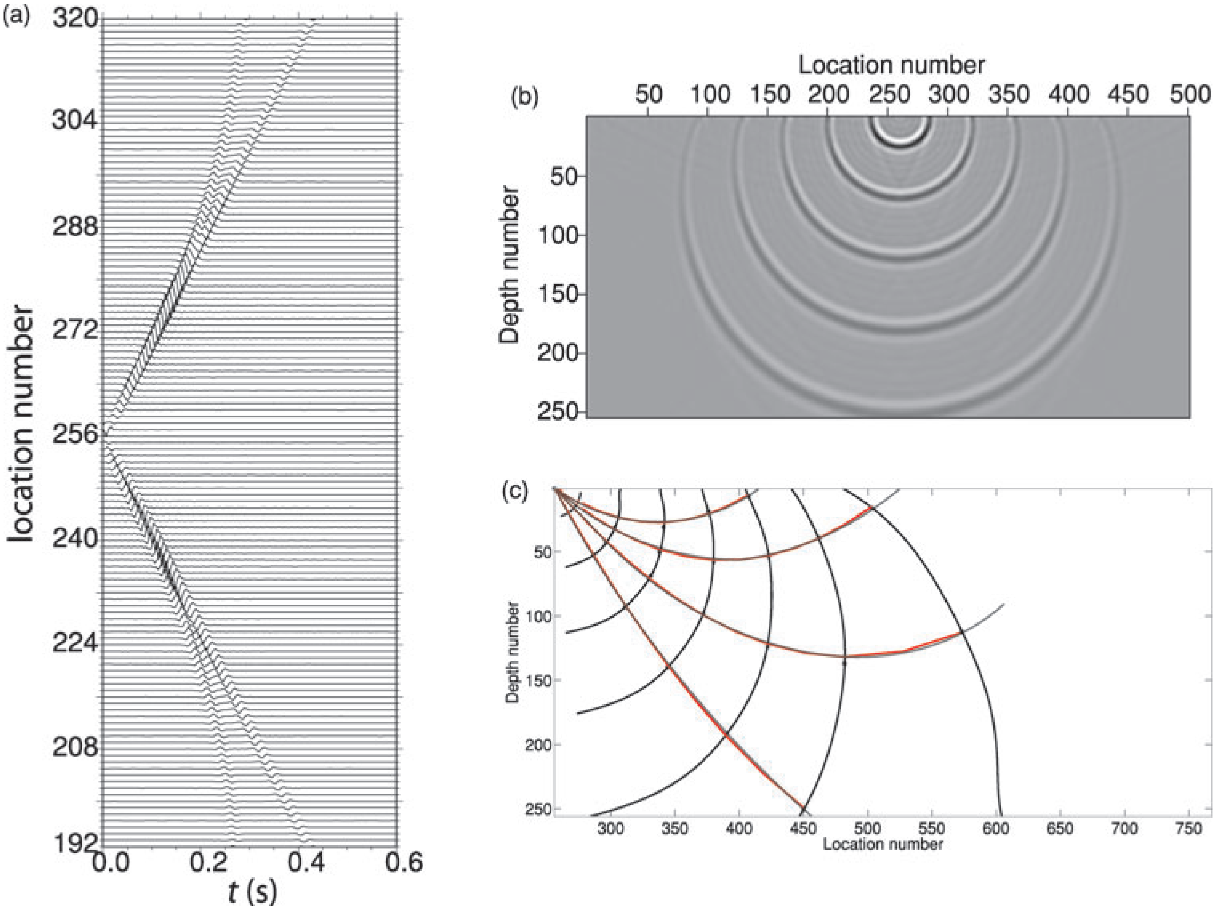

Figure 2. Modelling results of the superwide-angle GSP, which uses the wavefield gradient to calculate the propagation angle. The model is a strong velocity-gradient model. (a) Seismogram recorded by a split-spread survey on the surface. The source location number on the surface is 256. The direct arrivals have been weakened to render the signals of turning waves more clearly. (b) Snapshots for the traveltimes of 0.2, 0.35, 0.5, 0.65 and 0.8 s. (c) Wave fronts (black lines) picked from the snapshots and the turning rays (red lines) calculated by eq. (9). Two more wave fronts for 0.95 and 1.1 s are shown. The ray tracing results (grey lines) are also shown for comparison.

For dual-domain propagators such as the GSP, the thin-slab propagator and the beamlet propagator, the wavefield at a given space point is usually a complex number. This is the reason we use absolute values in eq. (7). However, the propagation angle will always be non-negative in this way. For a downward propagator, for example, it is still unknown whether the wavefield propagates left or right with the propagation angle given by eq. (7).

In the dual-domain methods, the wavefield is switched between the space domain and the wavenumber domain by Fourier transform. In the wavenumber domain, according to the sign of the transverse wavenumber, we can easily separate the left and the right side components of the downward propagated wavefield, denoted as $u_L(k_x < 0, z)$ and $u_R(k_x > 0, z)$, respectively. By transforming them back to the space domain, we have $u_L(x, z)$ and $u_R(x, z)$ at any space point. If $|u_L(x, z)|$ is larger than $|u_R(x, z)|$, we believe that the wavefield at (x, z) propagates left, and vice versa.

If the propagator is implemented only in the space domain, eq. (7) should be modified as

$$\theta\,(x, z) = \tan^{-1}\left(\frac{\partial u}{\partial x}\bigg/\frac{\partial u}{\partial z}\right). \tag{8}$$

In this case, the wavefield at a specified point is a real number and the propagation angle given by eq. (8) can make difference between left and right propagations.

Provided with the wave propagation angle, we also have the ray parameter as

$$p\,(x, z) = \frac{\sin\theta}{c}, \tag{9}$$

where c is the velocity of the medium.

In the 3-D case, the wavefield gradient has three components. As in the 2-D case, the components can be calculated simply by the finite difference approximation. Alternatively, we can still derive the gradient expression from the marching equation of the one-way propagator. Taking both the accuracy and the cost into account, the finite difference approach is recommended to calculate the wavefield gradient in the 3-D case. Once the wavefield gradient is obtained, the propagation angles (i.e. the angle with respect to the vertical direction and the azimuth angle) can be determined similarly as in the 2-D case.

3 SYNTHETIC EXPERIMENTS

The approach of calculating the wave propagation angle with the wavefield gradient can be used in some dual-domain directional problems. It is applicable to most wave propagators. Here we show some applications of this approach to illumination analysis, seismic modelling and imaging. In the following examples, we use the Padé GSP for wavefield calculations.

3.1 Multifrequency analysis of the propagation angle

Frequency-dependent experiments and analyses provide accurate and detailed multiscale and multidepth subsurface information. The multifrequency analysis is an effective tool for seismic attenuation (Brajanovski *et al*. 2006) and diffraction tomography (Wu & Toksöz 1987). In this section, we illustrate some multifrequency results of the propagation angle obtained with wavefield gradients.

The velocity model under consideration is the A–A′ profile of the SEG/EAEG salt model shown in Fig. 1(a). Point sources are distributed evenly on the entire surface and explode simultaneously to generate a straight downward plane wavefield. The dominant frequency of the source signal is 15 Hz. Assuming $\theta(x, z)$ is the propagation angle of the wavefield at a given point (x, z), Fig. 1 shows the calculation results of $\cos\theta$ for five frequencies. In Fig. 1, we see clearly that the wavefields close to the salt boundary as well as in the salt body do not propagate in the vertical direction. The subsalt wavefields have more complicated propagation directions, especially for relatively high frequencies. The angle resolution of the low-frequency result is much lower than that of the high-frequency result. Illumination analysis and snapshot simulation confirm these results. Note that there are some knot-like anomalies in the result of very low frequency as Fig. 1(b) shows. In this case, the discrete scheme used for the calculation of the wavefield gradient may break down. The gradient calculation is likely in the scale less than one wavelength if the grid interval is not large enough. This will lead to an incorrect result, which does not represent the real wavefield gradient.

3.2 Turning wave modelling and imaging

Traditional one-way wave propagators cannot simulate turning waves, which propagate downward first and have been curved upward in the media with a vertical velocity gradient. Turning waves are useful in migration of some special features such as overhanging salt flanks and subsalt reflectors. To take this advantage, a superwide-angle one-way propagator (Jia & Wu 2007) has been developed, jointly using two orthogonally propagated one-way waves to rebuild the wavefield. For the combination of the two one-way waves, a pair of weights depending strictly on the propagation angle are required. Therefore, the calculation of the propagation angle is one of the key points in the superwide-angle one-way method. Here we show some examples of turning wave modelling and imaging with the superwide-angle one-way propagator, which employs our method to calculate the propagation angle.

The velocity-gradient media are sufficient for the turning wave to be generated. Fig. 2 shows the modelling results in a velocity-gradient model with the superwide-angle GSP method which uses eqs (5)–(7) to calculate the propagation angle. For the model, the space interval is 10 m, the velocity at the surface is 2 km s^{-1} and the vertical velocity gradient is 1.57 s^{-1}. We use a point source on the surface for the simulation. The dominant frequency of the source signal is 30 Hz. Fig. 2(a) shows the synthetic seismogram recorded by a split-spread acquisition survey. There are mainly two seismic events in it—the strong direct arrival and the turning wave. The latter cannot be simulated by the traditional GSP due to the angle limitation. In Fig. 2(a), the turning wave on the near-offset traces reaches the surface almost at the same time as the direct arrival. For far-offset traces, the difference between the traveltimes of the two waves becomes remarkable and the turning wave arrives earlier than the direct wave. Fig. 2(b) shows the snapshots at five traveltimes. The direct arrival is restrained within a very limited depth range beneath the surface. The split of the turning wave and the direct arrival near the surface can be easily recognized. With the amplitude maxima picked from the snapshots, we have the dominant phases of the turning wave shown in Fig. 2(c). The turning rays, which are calculated from eq. (9), are illustrated additionally. We also show the result of ray tracing for comparison. The rays obtained with two methods agree well with each other.

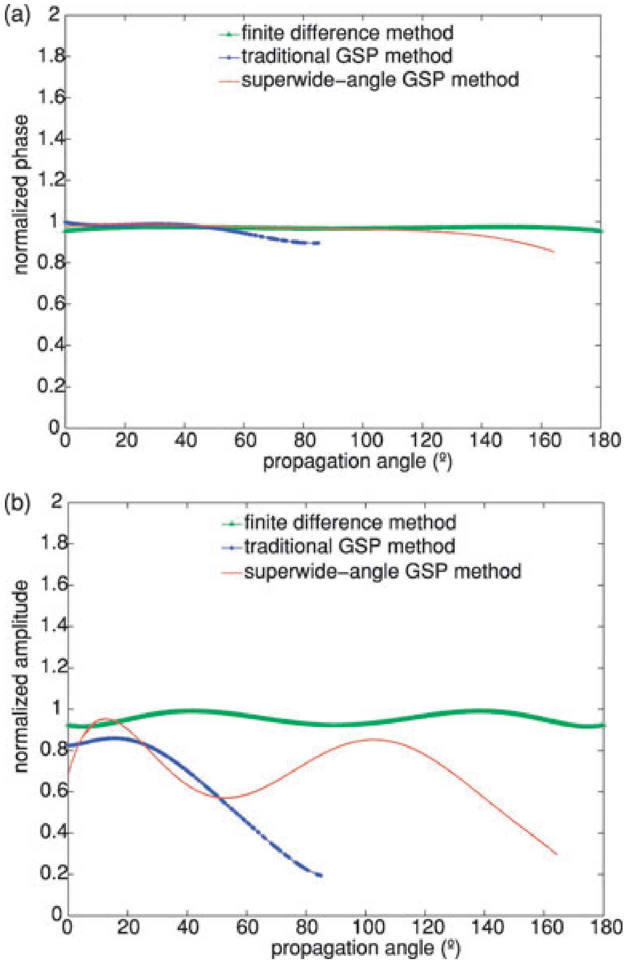

Figure 3. Comparisons of the phase and amplitude for the single-time snapshots obtained by three methods. The velocity model is a homogeneous model. (a) Normalized phase. (b) Normalized amplitude.

To see the advantage of our method in modelling superwide-angle waves more clearly, another quantitative experiment is conducted. The velocity model is a homogeneous model. Ideally, the snapshot at a single time should be obtained as a circle-like wave front around the point source. Here we calculate the snapshot with three methods—the finite difference, the traditional GSP and the superwide-angle GSP. For the latter two methods, we use a velocity perturbation of 50 per cent. Fig. 3 compares the normalized phase and amplitude of the snapshots. Due to the angle limitation, the traditional GSP fails to model the waves with propagation angle larger than 90°. The phase and amplitude errors are significant in the case of large propagation angles. However, the superwide-angle GSP, which employs our method to determine the propagation angle, leads to much less error in both phase and amplitude.

Now we proceed to a more complex model. Fig. 4 shows the 2004 BP 2-D benchmark velocity model for the zone of interest. The background sediments are characterized by an approximately vertical velocity gradient. Fig. 5(a) shows the snapshots of nine

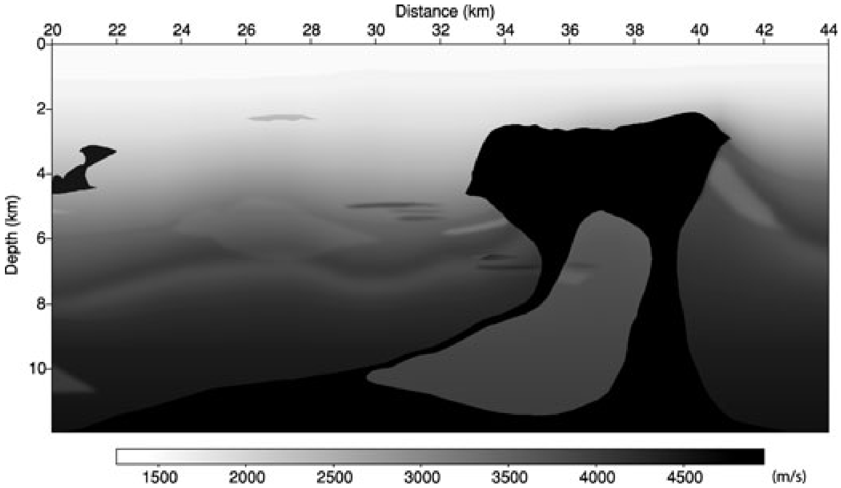

Figure 4. Velocity model of the 2004 BP 2-D benchmark data set. The velocity unit is m s^{-1}.

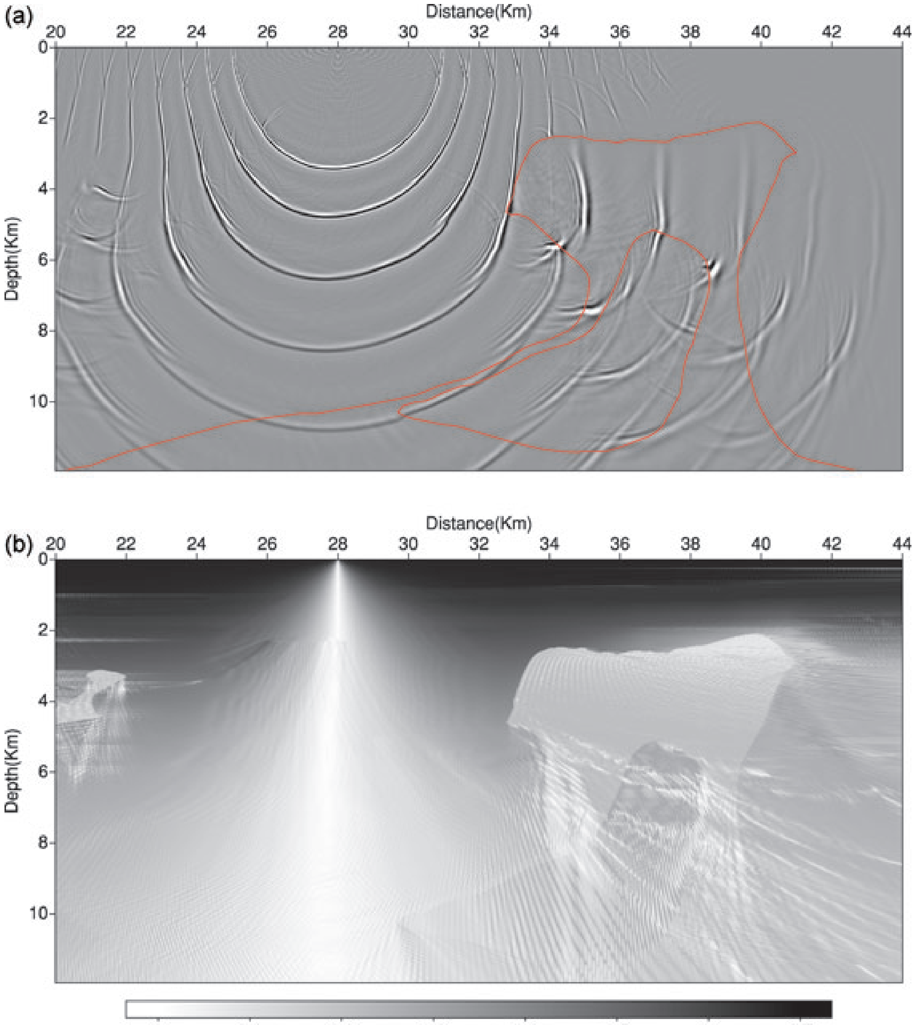

Figure 5. Modelling results of the superwide-angle GSP, which uses the wavefield gradient to calculate the propagation angle. The model is shown in Fig. 4 and the source is located at (28 km, 0). (a) Snapshots for the traveltimes of 2.0, 2.5, 3.0, 3.5, 4.0, 4.5, 5.0, 5.5 and 6.0 s. The contour of the salt body is sketched. (b) Distribution of the ray parameter for the frequency of 27 Hz. The unit is s km^{-1}.

traveltimes using the superwide-angle GSP. The shot is located at the surface and the dominant frequency is 27 Hz. Note the phases concerned with the reflected turning waves near the left flank of the salt dome. For the dominant frequency, Fig. 5(b) shows the distribution of the ray parameter calculated from eq. (9). Due to the existences of strong velocity contrast and small-scale anomalies, the distribution of the ray parameter around the salt boundaries is quite complex. However, we can still observe the trend of the turning wave incident and reflected on the left flank of the salt.

By using the wavefield gradient to determine the wave propagation angle, the superwide-angle GSP simulates the turning wave well. Therefore, it can be applied to image some special features such as overhanging structures. Here we implement the superwide-angle GSP migration as well as the traditional GSP migration for the overhanging salt flank located on the upper left boundary of the salt dome in Fig. 4. We use 50 single shot gathers for migration. The receiver array is on the left-hand side of the shot with the array length of 15 km. The shot interval is 100 m and the receiver interval is 12.5 m. The dominant frequency of the data is 27 Hz. Fig. 6 shows the comparison between single shot images obtained by different methods. The image of traditional GSP, shown in Fig. 6(a), presents very little energy on the overhanging salt flank under consideration. In contrast, the energy is well restored in the image of the regular superwide-angle GSP method, displayed in Fig. 6(b). However, there is too much noise decreasing the resolution of the image. The artefacts are caused mainly by inaccurate calculations of the propagation angles in the superwide-angle GSP method. With the help of the approach proposed in this paper, as Fig. 6(c) shows, the superwide-angle GSP migration produces an image with much higher signal-to-noise ratios. Most of the noise is removed and some reflectors absent in Fig. 6(b) are visible. To see this point more clearly, Fig. 7 shows the corresponding stacked

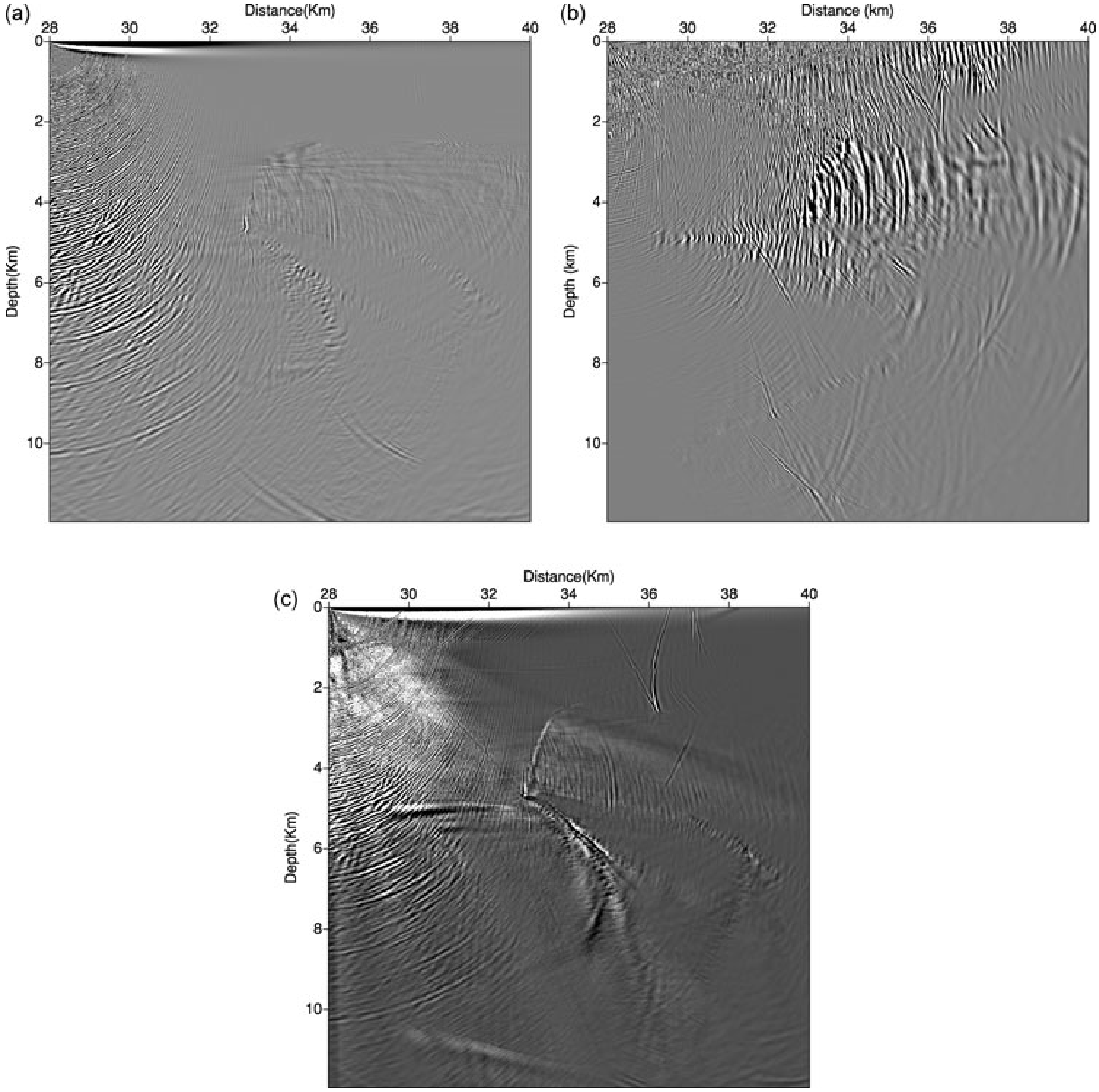

Figure 6. Single-shot imaging results. The model is shown in Fig. 4 and the shot location is (28 km, 0). (a) Image obtained by the traditional GSP migration. (b) Image obtained by the regular superwide-angle GSP migration. (c) Image obtained by the superwide-angle GSP migration which uses the wavefield gradient to calculate the propagation angle.

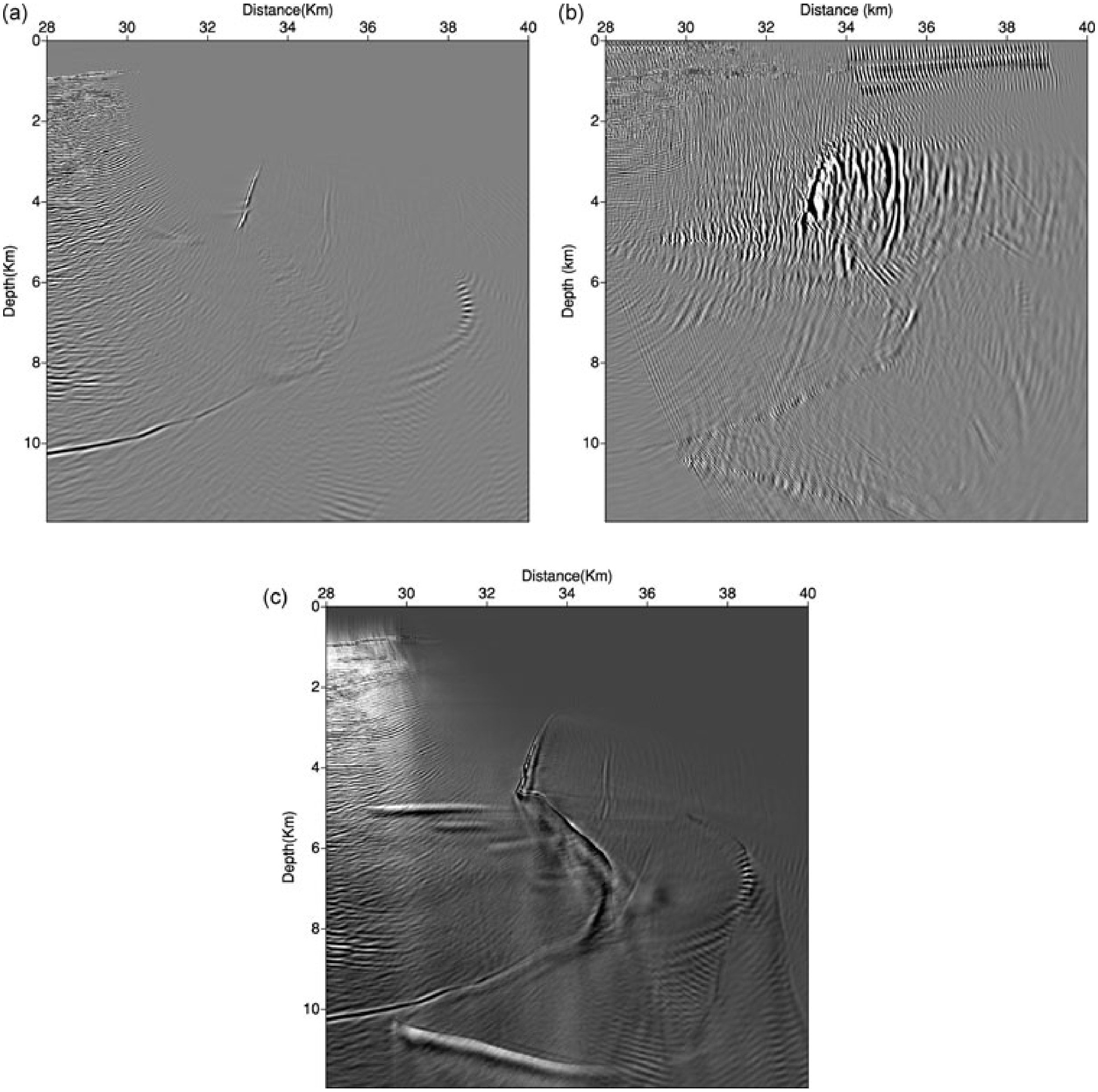

Figure 7. Stacked imaging results. The model is shown in Fig. 4 and the shot locations range from 25 to 29.9 km on the surface. (a) Image obtained by the traditional GSP migration. (b) Image obtained by the regular superwide-angle GSP migration. (c) Image obtained by the superwide-angle GSP migration which uses the wavefield gradient to calculate the propagation angle.

images. Compared with the result from the traditional method, the image of the superwide-angle method has much better quality, due to dealing with turning waves successfully. This advantage is enhanced by applying our method of calculating the propagation angle to the superwide-angle migration.

4 CONCLUSIONS

The wave propagation angle provides a useful tool for seismic modelling and migration concerned with some special events such as turning waves. A direct and easy approach to obtain the wave propagation angle in the space domain is implemented by using the wavefield gradient, which indicates the direction of the energy flow. This method is especially effective for the dual-domain propagators since it is usually difficult to get the propagation angle at a specified point in the space-frequency domain.

The superwide-angle one-way propagator, which needs accurate calculation of the wave propagation angle, has great advantages over the traditional one-way propagator in the aspect of steep reflector imaging. Combined with the approach of deriving the angle by the wavefield gradient, the superwide-angle one-way propagator can simulate turning waves well and consequently yield high-quality images of overhanging structures. The proposed approach does not come without any cost. In the case of very low frequency, the calculation of the wavefield gradient is processed in the scale of less than one wavelength, which leads to invalid results.

ACKNOWLEDGMENTS

The authors thank BP for providing the 2004 BP 2-D data set. We are grateful to Prof. Jean Virieux and two anonymous reviewers for their constructive comments. This paper also benefits from the helpful discussions with Jun Cao and Hui Yang. The supports from the Wavelet Transform On Propagation and Imaging (WTOPI for seismic exploration) Research Consortium and the DOE/BES Project at the University of California, Santa Cruz are acknowledged.

REFERENCES

Aki, K. & Richards, P., 1980. *Quantitative Seismology: Theory and Methods*, Freeman, San Francisco.

Biondi, B. & Symes, W.W., 2004. Angle-domain common-image gathers for migration velocity analysis by wavefield-continuation imaging, *Geophysics,* **69,** 1283–1298.

Brajanovski, M., Müller, T.M. & Gurevich, B., 2006. Characteristic frequencies of seismic attenuation due to wave-induced fluid flow in fractured porous media, *Geophys. J. Int.,* **166,** 574–578.

Bruneton, M., Farra, V., Pedersen, H.A. & the SVEKALAPKO Seismic Tomography Working Group, 2002. Non-linear surface wave phase velocity inversion based on ray theory, *Geophys. J. Int.,* **151,** 583–596.

Carcione, J.M., 1997. Reflection and transmission of *qP-qS* plane waves at a plane boundary between viscoelastic transversely isotropic media, *Geophys. J. Int.,* **129,** 669–680.

Castagna, J.P., Batzle, M.L. & Kan, T.K., 1993. Rock physics: the link between rock properties and AVO response, in *Offset-dependent reflectivity: Theory and Practice of AVO Anomalies,* Investigations in Geophysics, no. 8, pp. 135–171, eds Castagna, J.P. & Backus, M.M., Soc. Expl. Geophys., Tulsa.

Cerveny, V., 2001. *Seismic Ray Theory,* Cambridge University Press, Cambridge.

Cerveny, V. & Psencik, I., 2006. Energy flux in viscoelastic anisotropic media, *Geophys. J. Int.,* **166,** 1299–1317.

Crampin, S., Stephen, R.A. & McGonigle, R., 1982. The polarization of *P*-waves in anisotropic media, *Geophys. J. Int.,* **68,** 477–485.

Fomel, S., 2002. Applications of plane-wave destruction filters, *Geophysics,* **67,** 1946–1960.

Fujiwara, S., Ozawa, S., Murakami, M. & Tobita, M., 2000. Estimation of fault positions of the 1995 Hyogo-ken Nanbu earthquake using surface displacement gradient detected by SAR interferometry, *J. Seismol. Soc. Jpn.,* **53,** 127–136.

Gray, S., 2006. Angle gathers for Gaussian beam depth migration, in *Proceedings of the 2006 CSPG, CSEG, CWLS Joint Convention,* Expanded Abstracts, pp. 75–81.

Jia, X. & Hu, T., 2006. Element-free precise integration method and its applications in seismic modelling and imaging, *Geophys. J. Int.,* **166,** 349–372.

Jia, X. & Wu, R.S., 2007. Imaging steep salt flanks by super-wide angle one-way method, in *Proceedings of the 77th Ann. Int. Mtg., SEG*, Expanded Abstracts, pp. 2265–2269.

Jones, K.A., Warner, M.R., Morgan, R.P.L., Morgan, J.V., Barton, P.J. & Price, C.E., 1996. Coincident normal-incidence and wide-angle reflections from the Moho: evidence for crustal seismic anisotropy, *Tectonophysics,* **264,** 205–217.

Legrand, D., 2003. A short note on the selection of the fault plane, the seismic moment tensor, the strain and rotational tensors, and the gradient of displacement, *Bull. seism. Soc. Am.,* **93,** 946–947.

Mandal, B. & Toksöz, M.N., 1990. Computation of complete waveforms in general anisotropic media—results from an explosion source in an anisotropic medium, *Geophys. J. Int.,* **103,** 33–45.

Nelson, D.F., 1996. Generalizing the Poynting vector, *Phys. Rev. Lett.,* **76,** 4713–4716.

Newman, P. & Mahoney, J.T., 1973. Patterns with a pinch of salt, *Geophys. Prospect.,* **21,** 197–219.

Ostrander, W.J., 1984. Plane-wave reflection coefficients for gas sands at non-normal angles of incidence, *Geophysics,* **49,** 1637–1648.

Rickett, J.E. & Sava, P.C., 2002. Offset and angle-domain common image-point gathers for shot-profile migration, *Geophysics,* **67**, 883–889.

Roberts, G.A. & Goulty, N.R., 1990. Directional deconvolution of marine seismic reflection data: north sea example, *Geophys. Prospect.,* **38,** 881–888.

Ruud, B.O., 2006. Ambiguous reflection coefficients for anelastic media, *Stud. Geophys. Geod.,* **50,** 479–498.

Ursin, B., de Hoop, M.V., Brandsberg-Dahl, S. & Sollid, A., 2005. Seismic angle migration, *Leading Edge,* **24,** 637–640.

Vines, R.E., Tamura, S. & Wolfe, J.P., 1995. Surface acoustic wave focusing and induced Rayleigh waves, *Phys. Rev. Lett.,* **74,** 2729–2732.

Wapenaar, K., van Wijngaarden, A.J., van Geloven, W. & Van Der Leij, T., 1999. Apparent AVA effects of fine layering, *Geophysics,* **64,** 1939–1948.

Wu, R.S. & Chen, L., 2006. Directional illumination analysis using beamlet decomposition and propagation, *Geophysics,* **71,** S147–S159.

Wu, R.S. & Toksöz, M.N., 1987. Diffraction tomography and multisource holography applied to seismic imaging, *Geophysics,* **52,** 11–25.

Xie, X.B. & Wu, R.S., 1998. Improve the wide angle accuracy of screen method under large contrast, in *Proceedings of the 68th Ann. Int. Mtg., SEG,* Expanded Abstracts, pp. 1811–1814.

Xie, X.B., Jin, S. & Wu, R.S., 2006. Wave-equation-based seismic illumination analysis, *Geophysics,* **71,** S169-S177.

Yoon, K. & Marfurt, K.J., 2006. Reverse-time migration using the Poynting vector, *Geophys. Explor.,* **59,** 102–107.

Zhang, Y., Xu, S., Bleistein, N. & Zhang G., 2007. True-amplitude, angle-domain, common-image gathers from one-way wave-equation migrations, *Geophysics,* **72,** S49–S58.